Temporal relationship of slow slip events and microearthquake seismicity: Insights from earthquake automatic detections in the northern Hikurangi margin, Aotearoa New Zealand

Jefferson Yarce[1,2], Anne F. Sheehan[1], Steven Roecker[3]

[1] Cooperative Institute for Research in Environmental Sciences and Department of Geological Sciences, University of Colorado Boulder, Boulder, CO, USA
[2] Now at Department of Earth and Environmental Sciences, University of Michigan, Ann Arbor, MI, USA
[3] Department of Earth and Environmental Sciences, Rensselaer Polytechnic Institute, Troy, NY 12180, USA

Key points

- We used an automatic detector and locator of earthquakes for an ocean bottom seismic dataset from offshore New Zealand.
- The automated method provides a three-fold increase in detections compared to manual picking
- The newly built database allowed us to observe an increase in seismicity during the 2014 slow slip event (SSE) in the Hikurangi margin.

Plain language summary

While most tectonic plates move at very slow speeds, two other types of motion are known: the rapid plate movement of an earthquake, where a plate moves by centimeters to meters in a few seconds, and a more puzzling type of motion in which a plate moves a similar distance but over weeks to months. This latter movement is called a 'slow slip event' and is known to occur in subduction zones around the world. We still do not understand the relationship between slow slip events and earthquakes. To explore this interaction, we used automatic detection of earthquakes in data collected from the seafloor overlying a known region of slow slip movement near New Zealand. We were then able to build a catalog of earthquakes that is more consistent and over three times larger than the number of earthquakes detected by human analysts. With this new set of seismic events, we found that the occurrence of small earthquakes increased during a 2014 slow slip event and returned to their baseline gradually after the slow slip stopped, suggesting a link between the processes that lead to these enigmatic slow-motion earthquakes and the more typical earthquake motions.

Abstract

Slow slip events in the northern Hikurangi margin of Aotearoa New Zealand occur every 18 to 24 months and last for several weeks before returning to average rates of convergence of around 38 mm/yr.

This is the author manuscript accepted for publication and has undergone full peer review but has not been through the copyediting, typesetting, pagination and proofreading process, which may lead to differences between this version and the Version of Record. Please cite this article as doi: 10.1029/2022GC010537.

Along this plate boundary, the Hikurangi plateau subducts beneath the overlying Australian plate and slow slip events occur along their plate interface at depths between 2 and 15 km. To explore whether there is a temporal relationship between slow slip events and earthquake occurrence, the Regressive ESTimator (REST) automated phase arrival detection and onset estimation algorithm was applied to a dataset of continuous waveform data collected by both land and ocean bottom seismometers. This detector uses an autoregressive algorithm with iterative refinement to first detect seismic events and then create a catalog of hypocenters and P and S wave arrival times. Results are compared with an available catalog of manually-detected seismic events. The auto-detector was able to find more than three times the number of events detected by analysts. With our newly assembled dataset of automatically detected earthquakes, we were able to determine that there was an increase in the rate of earthquake occurrence during the 2014 slow slip event.

1 Introduction

Displacements along plate boundaries in subduction zones around the world are generally accommodated through deformation in the form of continuous aseismic creep (on the order of cm/yr) or sudden strain release in earthquake ruptures (on the order of meters per second) (Schwartz & Rokosky, 2007). With the advent of continuous GNSS networks over the last two to three decades that record crustal deformation in subduction zones, a new type of tectonic motion called Slow Slip Events (SSEs) was discovered whereby episodic slips occur at a faster rate than continuous aseismic creep but slower than seismic events (Dragert et al., 2001; Schwartz & Rokosky, 2007). SSEs show displacements of tens of centimeters that span a timeframe of weeks to even tens of years (Schwartz & Rokosky, 2007). Although SSEs have been studied numerically, in the laboratory, and at field sites at various subduction zones, the relationship between SSEs and seismicity remains unclear. Some of these studies have shown that there can be an increase in the number and frequency of earthquake occurrences during SSEs relative to background seismicity (Colella et al., 2017; Vallée et al., 2013). Laboratory experiments have suggested that the occurrence of SSEs may promote coseismic slip on their host fault (Ikari, 2019). Additionally, Ito et al.

(2013) determined that an SSE triggered moderate interplate earthquakes and preceded the largest foreshock of the 2011 Tohoku-Oki earthquake. Although these laboratory and field-based results are suggestive, the potential connection between SSEs and seismicity requires additional investigation.

An ideal target to investigate SSE-seismicity linkages is a recurring and shallow SSE along the North Island of New Zealand. At the northern Hikurangi subduction margin, the westward Pacific plate converges with the North Island section of the Australian plate at an average rate of 4.5 cm/yr (Figure 1). This margin has frequent SSEs that take place every 18-24 months and last for a few weeks (Wallace, 2020; Wallace et al., 2016). One of these regular SSEs was targeted by a year-long temporary network of ocean floor pressure and seismic instruments deployed between June 2014 and May 2015 as part of the Hikurangi Ocean Bottom Investigation in Tremor and Slow Slip, or HOBITSS experiment (described in more detail in Yarce et al. (2019)). An approximately two-week SSE was successfully recorded geodetically from late September to early October 2014 (approximately September 23 – October 9, 2014). This offshore SSE had a maximum slip of 250 mm and occurred along the upper 15 km of the plate interface (Wallace et al., 2016; Figure 1). Overlying the displaced SSE area, the HOBITSS ocean bottom seismometers registered ground motions (including tremors and microearthquake seismicity) through the complete duration of the SSE. In conjunction with the permanent land seismic network operated by GeoNet, the HOBITSS record allows us to investigate the evolution of seismicity before, during, and after this 2014 SSE.

The temporal association of seismicity with the 2014 SSE was explored previously in land and ocean bottom seismic records using fully or partially hand-picked detection methods to identify seismic events. These studies allowed valuable insights into the understanding of the seismological characteristics of the northern Hikurangi margin throughout this 2014 SSE event. For example, Todd et al. (2018) discovered two tremor episodes that correlate spatially with both shallow subducted seamounts and the 2014 SSE areal displacement. These tremor episodes also temporally overlapped the SSE event and persisted for a couple of weeks after the SSE tapered off (Todd et al., 2018). Using HOBITSS and GeoNet data, we manually built a catalog of microearthquake seismicity and found that the seismicity rates increased at the start of the SSE and sustained elevated seismicity for two months after the end of the SSE

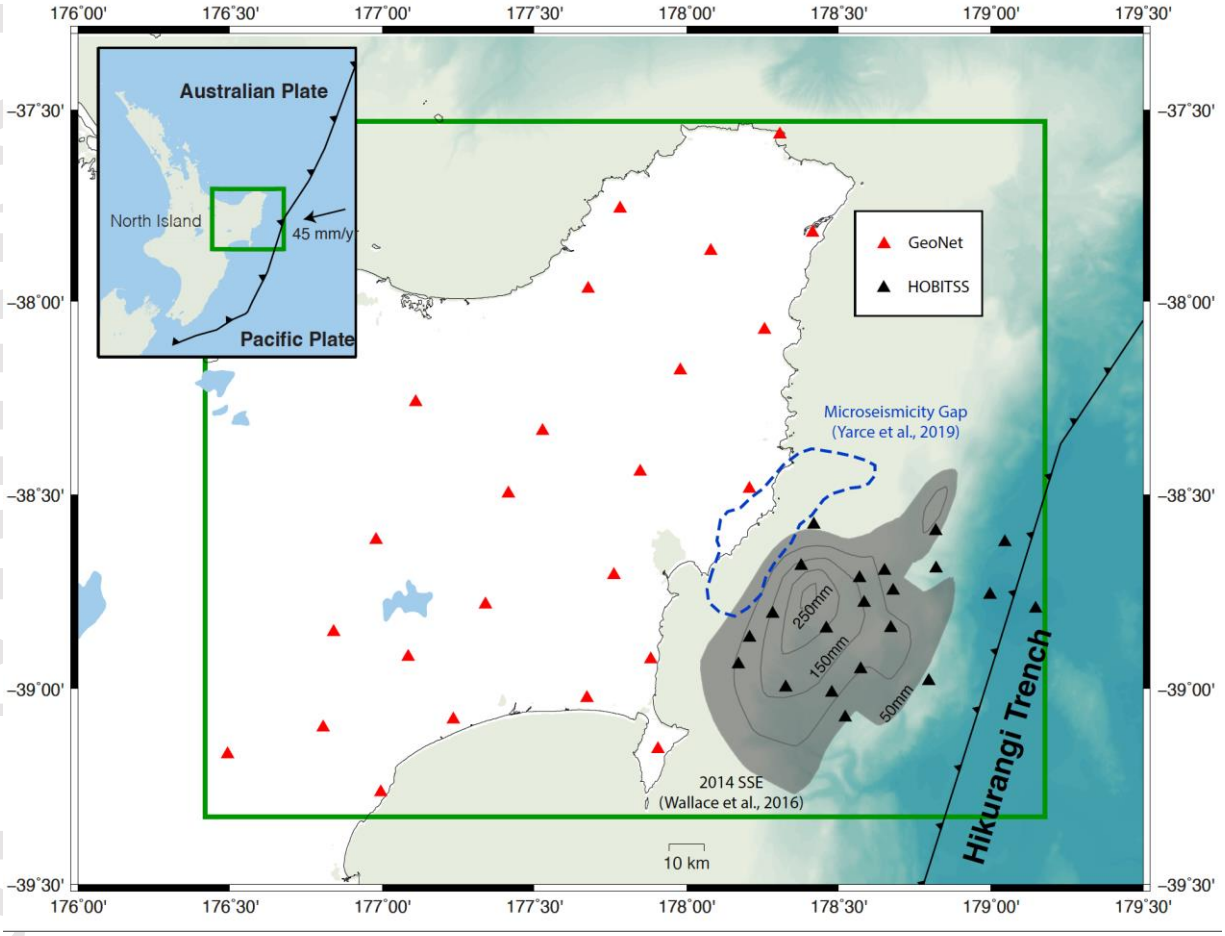

Figure 1: Location of study area in the North Island of New Zealand. Green rectangle outlines the limits of the 3D velocity model of Yarce et al. (2021) down to 94 km depth. Gray shaded patch with contours marks the region that was displaced during the September – October 2014 SSE. Contour interval is 50 mm as annotated (Wallace et al., 2016). Blue dashed line outlines the 2014-2015 microseismicity gap according to the manually built earthquake catalog in Yarce et al. (2019). Red and black triangles mark the location of GeoNet and HOBITSS seismometers, respectively. Inset map in top left shows the tectonic setting of the study area.

(Yarce et al., 2019). Shaddox and Schwartz (2019) applied an automated template-matching earthquake detection technique on the hand-picked microearthquake catalogs of Todd et al. (2018) and Yarce et al. (2019). Their results revealed repeating earthquakes located at the downdip edge of the subducted seamount towards the end of the 2014 SSE (Shaddox & Schwartz, 2019). These three studies demonstrated that temporal correlations exist between the 2014 SSE and the timing of Hikurangi margin seismicity. However, these investigations all use or have some connection to hand-picked seismicity records that are subject to inter- and intra-analyst biases and inconsistencies (Ross et al., 2018).

A more complete, uniform, and comprehensive catalog of earthquakes is wanted to accurately compare the seismicity record with the 2014 SSE timing. An automated catalog would provide consistency and repeatability and avoid analyst biases. Uniform and reliable wave phase arrivals in seismograms are crucial for hypocenter calculation and travel time inversions (Allam & Ben-Zion, 2012; Diehl et al., 2009; Di Stefano et al., 2006). Furthermore, temporal analyses of seismic features that may evolve with time could be affected by inherent errors in the manual process.

To detect earthquakes over a wide range of magnitudes, improve the manual earthquake catalog, and mitigate systematic bias by human analysts, we built a new automated catalog of earthquakes for the joint dataset of the ocean bottom and land seismometers during a time period spanning the 2014 SSE using the Regressive ESTimator (REST) algorithm for automated event detections, phase onset estimation, and hypocenter location (Comte et al., 2019; Thurber et al., 2017; Merrill et al., 2022). We created this catalog to (1) evaluate whether the use of an automatic catalog substantially expands the amount and quality of arrivals and event detections, and (2) further query the timing of seismicity before, during, and after the 2014 SSE.

2 Data and Methods

The HOBITSS experiment included an array of 15 ocean bottom seismometers deployed over the ocean floor from the abyssal plain near the subduction trench to the thick sedimentary wedge, ranging from around 3500 meters below sea level (mbsl) to as shallow as 650 mbsl (Figure 1). The land data are derived

from 24 broad band and short period permanent seismometers located on the North Island and operated by GeoNet (www.geonet.org.nz). For this study we selected 60 days of waveform data from the ocean bottom HOBITSS array together with terrestrial data from GeoNet. Specifically, we chose data from September 1st to October 31st, 2014 to include the two-week-long 2014 SSE. This subset of data was chosen to evaluate the seismicity in the days before, during, and after the 2014 SSE.

The identification of P- and S-wave arrivals in seismograms is fundamental to create a comprehensive catalog of earthquake hypocenters. An automated version of this process is carried out by the REST algorithm (Comte et al., 2019), which integrates an autoregressive estimation of seismic noise for signal detection and onset estimations (Pisarenko et al., 1987; Kushnir et al., 1990) with windowing and refinement schemes similar to those of Rawles & Thurber (2015).

The REST software produces an automatically detected catalog of P and S arrivals through iterative refinement of the onset estimations. Details of the algorithm are described elsewhere (e.g., Comte et al., 2019; Lanza et al., 2019). To summarize: the autoregression technique described in Kushnir et al (1990) is used to detect potential phase arrivals as any change (statistically defined) in a time series relative to background noise above a user-specified threshold. These detections are sorted chronologically and, if a sufficient number (in this case 4) occur withing a designated time window (e.g., one that would extend from the first P to the last S arrival for any event in the region of interest), a "potential event" is declared. The onset estimation procedure described in Pisarenko et al. (1987) is then used on the vertical components of windows of data from these potential events to identify potential P arrivals. If a viable hypocenter can be determined with some combination of available onsets by grid search (using procedures from Roecker et al., 2006) in an appropriate wavespeed model, an additional search is performed using windows based on arrival times predicted by that hypocenter. If that search is successful, the procedure is repeated two additional times with both horizontal components included to estimate onsets for S arrivals. If, at the end of these four iterations, a viable hypocenter is determined, the result is added to the catalog.

We employed REST to identify seismic events in an area covering the easternmost part of the North Island and the seafloor off the coast of Gisborne to the subduction trench (green rectangle in Figure 1),

using the Hikurangi margin 3D velocity model of Yarce et al. (2021). The initial search for detections examined seismograms using a single pass Bessel filter with a high-pass corner of 1 Hz and low pass corner equivalent to half the Nyquist frequency of the analyzed seismogram (Nyquist frequencies for instruments are 50 Hz for broadband seismometers and 100 Hz for the short period instruments). Following Comte et al. (2019), a successful identification of an earthquake was defined by the following criteria: (1) a minimum of 4 associated arrivals, (2) a travel time residual for each arrival of either less than 1.2 seconds or no larger than 4% of the total travel time, and (3) a standard deviation of travel time residuals less than 1 second.

When a sufficient number of reasonable quality waveforms are available, the REST algorithm can estimate Richter-type magnitudes by finding the maximum amplitude of the P coda (A) and the difference in arrival times of the P and S waves (dt). Often referred to as the local magnitude (M_L), the relation used is based on one defined for earthquakes in southern California:

$$M_L = a * log\ A\ + b * log\ dt\ - c, \qquad [1]$$

where a, b and c are regionally dependent constants that account for geometrical spreading, attenuation, and calibration of the local magnitude to the original Richter magnitude scale (Havskov & Ottemoller, 2010). The usual equivalent relation for New Zealand's local earthquake magnitude scale is stated by Ristau et al. (2016) as:

$$M_L = log\ A(R) + 1.49 * log\ R\ + (1.27 \times 10^{-3}) * R - 0.29\,, \qquad [2]$$

whereas R is hypocentral distance in kilometers. Effectively, the M_L definition for New Zealand is defined in terms of hypocentral distance, while the one used in REST is a function of difference in time between P and S (which serves as a proxy for distance). To translate REST-generated magnitude values into locally representative M_L, we performed a linear regression of the magnitudes computed by REST with the magnitudes of the same earthquakes computed in the manual catalog (Yarce et al., 2019) which used the New Zealand local magnitude computation (Figure 9). An additional correction was applied to account for differences in how instrument responses were applied, specifically the REST magnitude ($M_L old$) was found to relate to the the locally representative magnitude ($M_L new$) by:

$$M_L new = (M_L old * 0.83) - 0.14$$

Using this regression to produce a conversion factor, we were then able to compute a corrected magnitude for 421 of the earthquakes located using REST with values ranging between -0.4 to 3.2. With these magnitudes we evaluated the statistical characteristics of the microearthquake activity in the region using the frequency - magnitude distribution (or Gutenberg - Richter law). We used the goodness-of-fit method of Wiemer & Wyss (2000), to establish the b-value and magnitude of the completeness when the fitness of the distribution is at its maximum.

Table 1: Weighting factors by location of earthquakes relative to contours of slip (in mm) of the 2014 SSE contours.

Region of earthquakes	Weight	**Number of earthquakes in region**
Outside 50 mm contour	1	753
Within 50 and 100 mm	2	44
Within 100 and 150 mm	4	30
Within 150 and 200 mm	8	10
Within 200 and 250 mm	16	15
Within 250 mm	32	2

3 Results

The initial catalog created by applying REST to the two months of continuous waveforms discussed here resulted in 1,739 seismic events corresponding to 20,368 P and 16,891 S arrivals for a total of 37,259 arrivals. On average the seismic events registered 16 arrivals between P and S phases. For each station used in this study, the program identified a minimum of 571 and a maximum of 1500 P and S arrivals. By comparison, the manual catalog for the same time period consisted of 265 events with a total of 2,560 P

and S wave arrival times (Yarce et al., 2019). An example of an earthquake detected using REST that did not appear in the original catalog is shown in Figure 2.

We also found that of the 1,739 autopicked microearthquakes, 222 were also in our manually-picked catalog. The reasons for the non-detection of the 43 missed events are variable, but mostly result from the metrics used by REST to assess onset estimation quality (based mostly on the shape of the estimation function) which prevented a sufficient number of reasonable quality arrivals to be identified to allow determination of a hypocenter. Indeed, visual inspection of these events revealed that several of the manually detected P and S arrivals were not clear and in hindsight should not have been picked, and only 6 events out of those missing 43 events have greater than or equal to 10 arrivals.

As the initial catalog is likely to include poorly constrained locations, we applied additional criteria similar to those used in Comte et al. (2019) to develop a more robust and reliable catalog of hypocenters. Specifically, seismic events were culled from the initial set by requiring a minimum of 10 arrival times, with at least 2 S arrivals, and a location more than 3 km from the boundaries of the velocity model. This selection resulted in 853 earthquakes in the area bounded by the 3D velocity model of Yarce et al (2021).

We also evaluated the P and S wave arrival times from the set of 222 events identified in both manual and automated datasets. Results of this comparison showed that the difference between auto- and manually-picked P phases is no more than a few hundredths of a second (Figure 3), the automated picks are on average 0.062 seconds later. This DC offset is most likely a result of differences in phase delay due to the digital filters employed (both used bandpass filters between 3 and 8 Hz, but the manual picking used a two-pass IIR filter while REST uses a one-pass Bessel filter). We note that if the DC offset is removed from the P residuals, then 77% of the onset differences are less than 0.1 s and 91% are less than 0.2 By comparison, the differences between manual and automated S arrivals skew negative (i.e., automated picks are more often later) with an asymmetric distribution that has a longer negative tail (Figure 3). What the average difference is 0.25 seconds, most automated arrivals are about 0.15 seconds later, with about 67% of these arrivals being within 0.2 s of each other. S picks in general are less precise, but the reason for the negative skew is likely a consequence of how the picks are made. While the manual picks are generally

made on the more energetic horizontal component, REST considers both components simultaneously, and hence is less likely to pick S-P phase conversions that arrive prior to the main S phase.

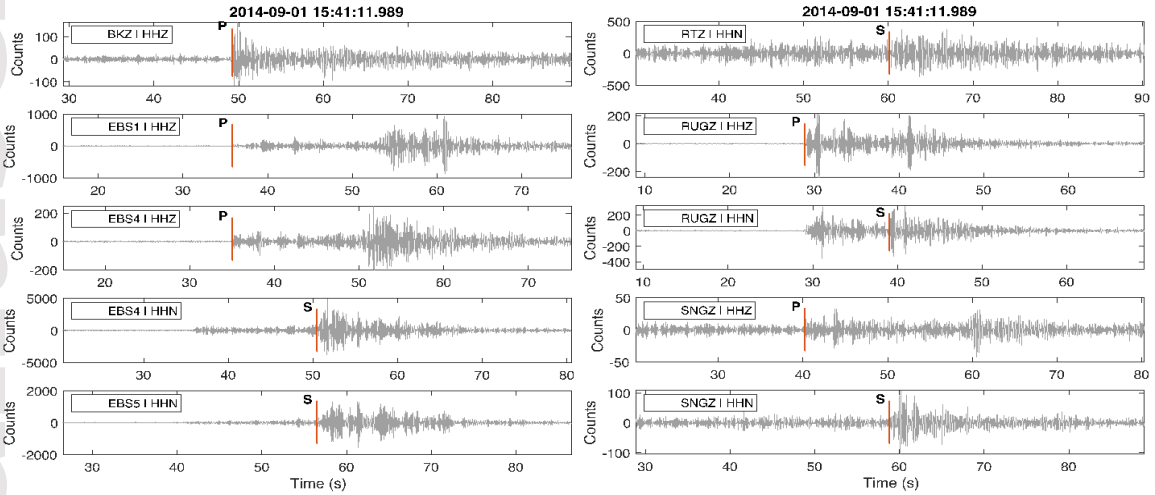

Figure 2: Example of a M_L 1.51 earthquake detected using REST and not detected previously using hand-picking of arrivals. P and S arrivals mark the auto-pick by REST (event id: 200007 in the catalog). Traces are bandpass filtered between 3 and 8 Hz.

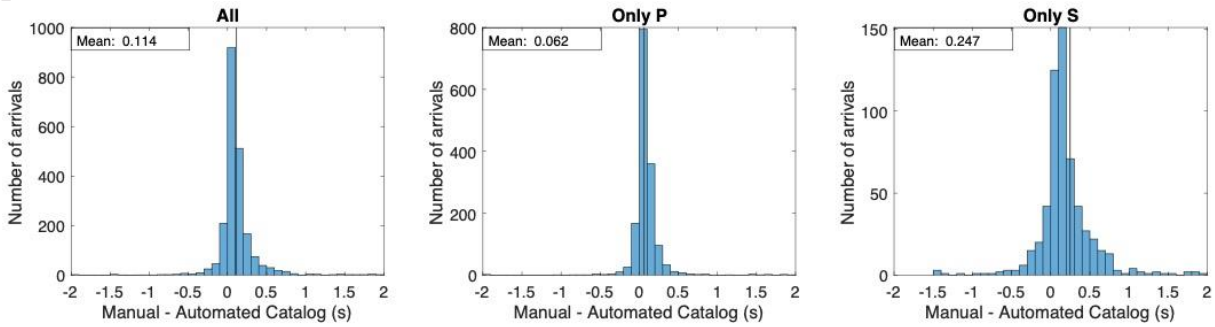

Figure 3: Time differences between common picks in manual vs. automated catalogs for events in common to both. The average of the residuals is shown with a solid grey vertical line.

With the use of a 3D velocity model (Yarce et al. 2021) in the automated catalog generation instead of the 1D velocity model of Yarce et al. (2019), changes were expected in the hypocenter locations of the 222 corresponding events. An analysis of the horizontal and vertical changes in hypocenter location shows that most of the hypocenters shift primarily to the west in the automated catalog, varying horizontally from 0 to 20 km (Figure 4a). The focal depth of these hypocenters changes by an average of 2.2 km towards shallower depths in the automated catalog (Figure 4b).

A map view of this final catalog of the selected 853 earthquakes (Figure 5) show their geographic relation to the microseismicity gap and 2014 SSE. A histogram of earthquake depths shows that hypocenter locations are predominantly shallow, with depths peaking between 20 and 25 km and at least 75% of the events occurring shallower than 35 km (Figure 6). Viewed in cross-section (Figure 7), these hypocenters appear unusually scattered. To test if this scatter is real, we applied a strict selection criteria, namely that the 2-sigma uncertainties derived from marginal probability distribution function for depth be less than 10 km, and compared those locations with the larger dataset. As the plot using this more restrictive subset (dark green circles in Figure 7) shows essentially the same amount of scatter, we conclude that it is most likely real. We note that offshore, the hypocenters are close to the plate interface, but also with depths as deep as 40 km. Onshore, the hypocenters are also located in the overlying continental plate with some clusters close to the plate interface. To demonstrate that the patterns in seismicity shown in Figure 7 are not

an artifact of absolute location methodology, we selected a subset of 249 of the better constrained locations, removed suspected outliers (based on absolute travel time residuals), and relocated them using the double-differencing and demeaning approaches described in Roecker et al. (2021). For these well-recorded events, the double-differenced locations did not change from the absolute locations significantly (in most cases by less than one kilometer). We find the same patterns, and in particular the apparent scatter in hypocenters, with the double-difference analysis as in the original locations shown in Figure 7.

To determine how these microearthquake hypocenters may spatially and temporally relate to the region that slipped during the 2014 SSE, we weighted hypocenter locations by their distance to the maximum slip (250 mm) of the SSE (see contours in Figure 1 and weight in Table 1). The results of this distance weighting scheme were then temporally averaged with a moving window of 4 days. The temporal distribution of the number of earthquakes per day is compared to the approximate start and end of the 2014 SSE as defined by GPS results (Figure 2 in Wallace et al. (2016)) (Figure 8a) and contrasted with a distance to slow slip area weighted count of number of earthquakes per day (Figure 8b).

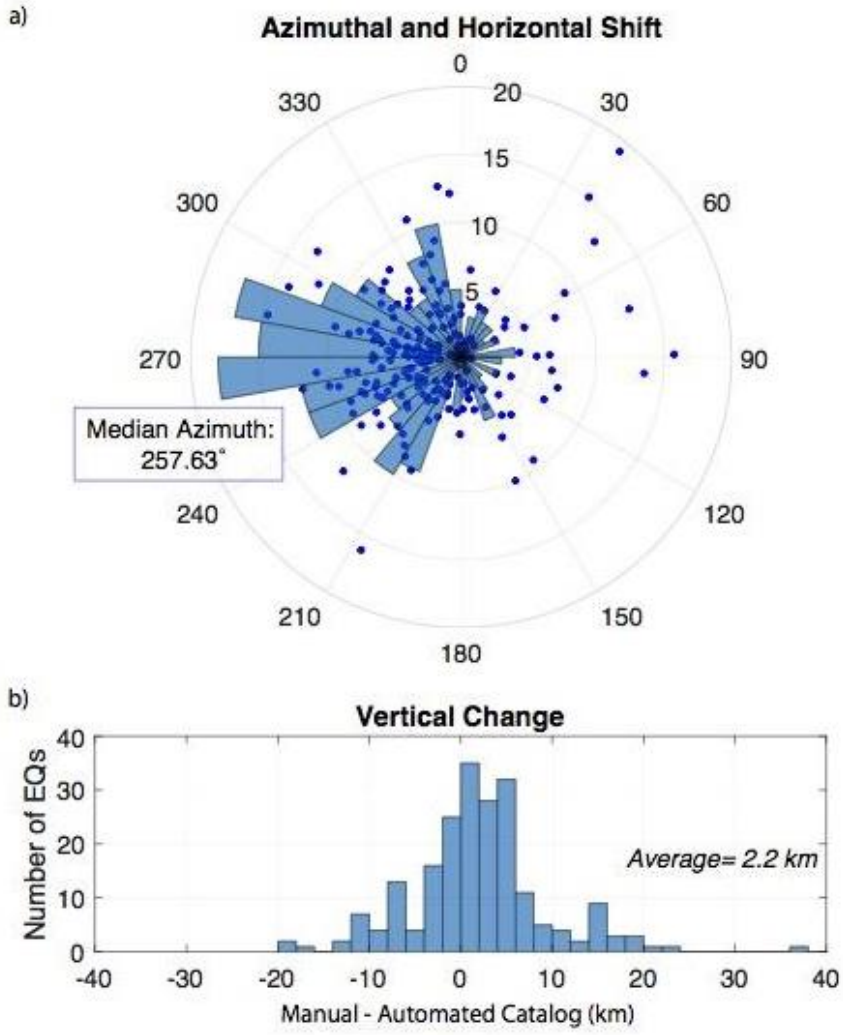

Figure 4: a) Polar plot of azimuthal and horizontal distance change from manual (center of polar plot) to automated catalog. Radial axis serves as both distance change (in km) and for number of earthquakes in azimuthal histograms in bins of 10 degrees. b) vertical changes between the manual and automated catalogs (for reference, a positive vertical change represents that the automated earthquake detection and location resulted in a shallower depth than the one calculated in the manual catalog of Yarce et al., (2019)).

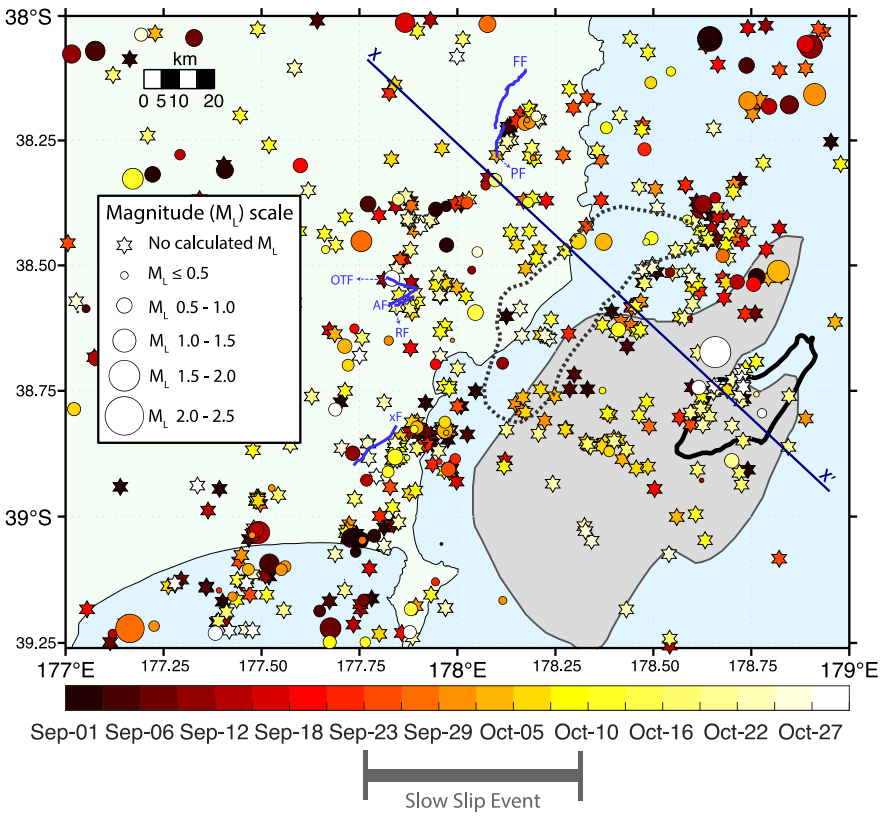

Figure 5: Map of earthquakes from September 1st to October 31st 2014 detected and located using REST. Earthquakes are color coded by onset time and sized according to local magnitude. Earthquakes without an estimated magnitude are plotted as a six-point star. Shaded gray is the area of the 2014 SSE that registered displacements of at least 50 mm (Wallace et al., 2016). Dotted black line outlines the microseismicity gap detected with the manual catalog (Yarce et al., 2019). Thick black line outlines a subducted seamount (Barker et al., 2018). Dark blue line (X-X') denotes the cross section in Figure 7. Blue lines denotes active faults in the region (Langridge et al., 2016): AF: Arakihi Fault, OTF: Otoko-Totangi Fault, RF: Repongaere Fault, PF: Pangopango Fault, FF: Fernside Fault, xF: unnamed fault.

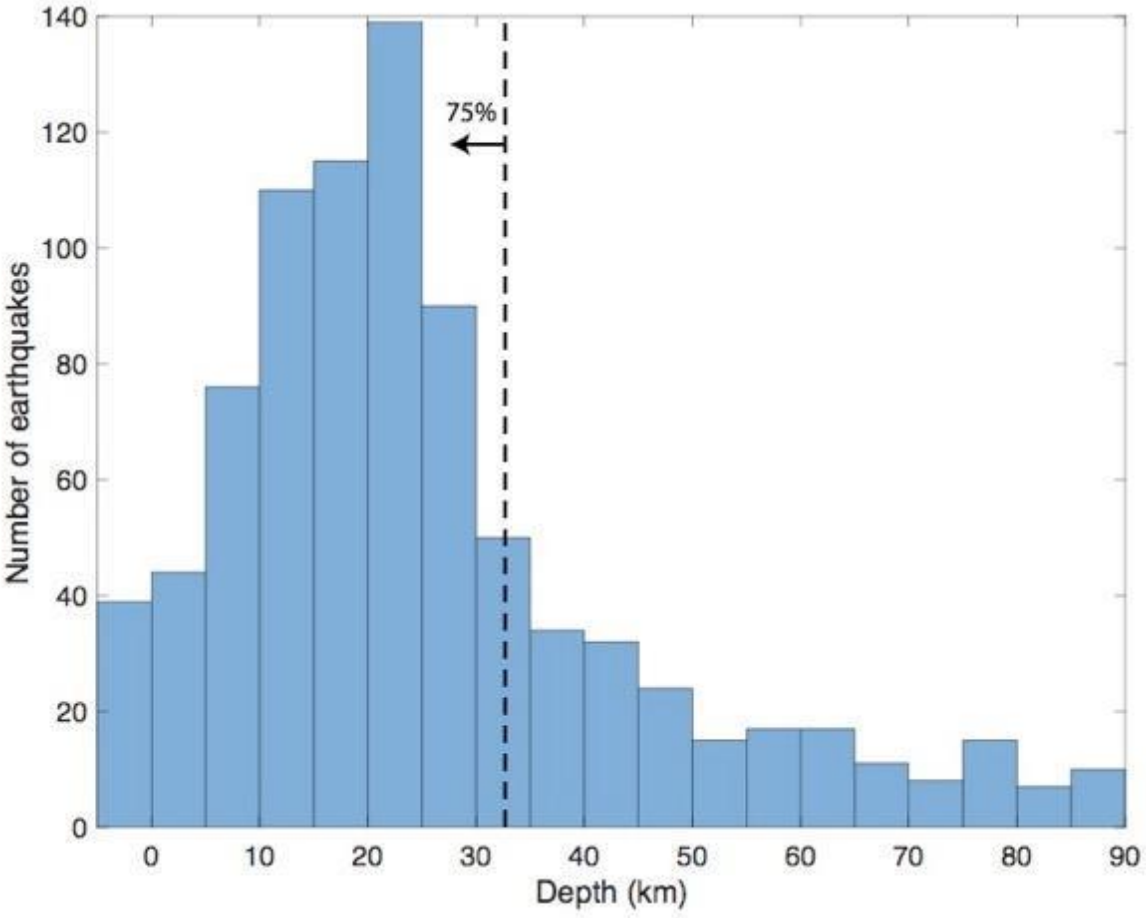

Figure 6: Histogram of earthquake depths for selected events. Dashed line marks the point where at least 75% of events are shallower than 35 km.

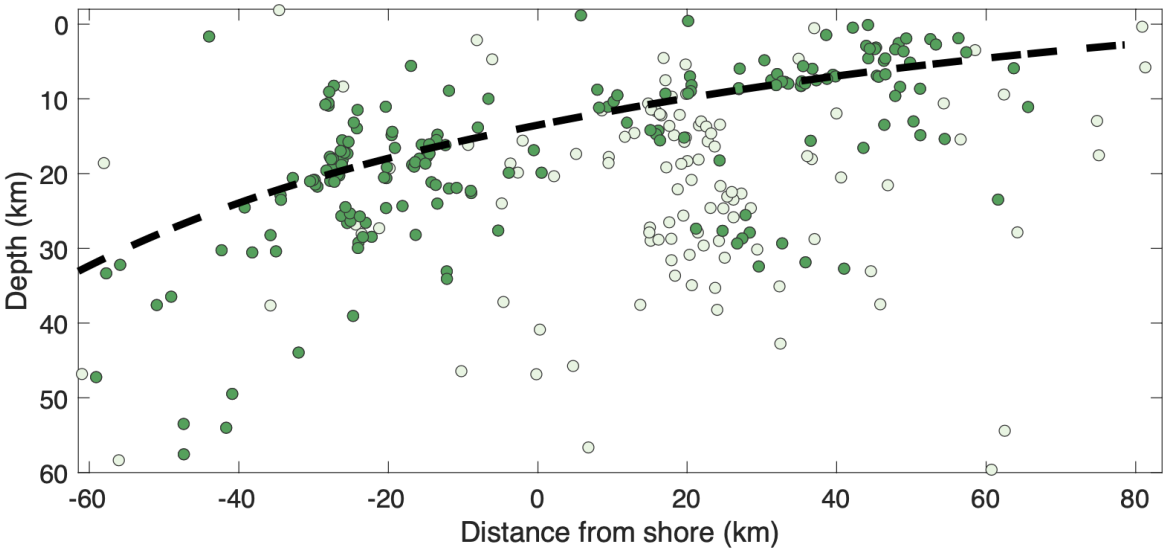

Figure 7: Cross-sectional view of earthquake hypocenters (circles) within 30 km of line X-X' in Figure 5 s. Dark green circles represent those earthquakes with 2-sigma depth uncertainties less than 10 km. Black dashed line is the projection of the plate interface from Williams et al. (2013).

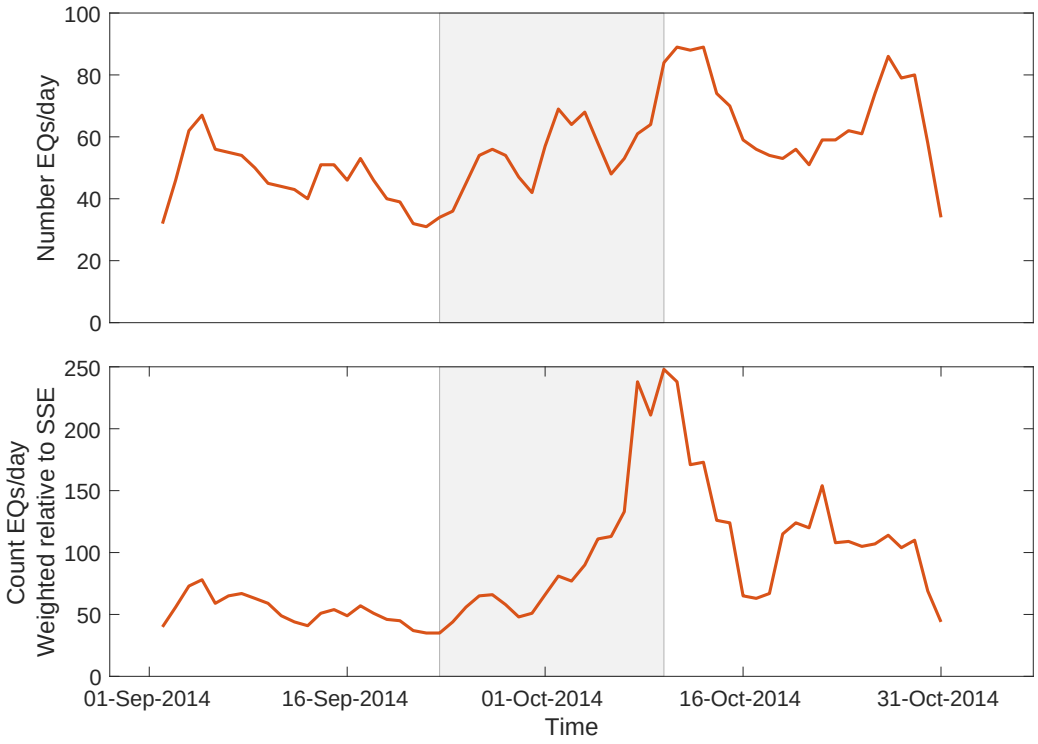

Figure 8: a) Moving sum of the number of earthquakes per day for the two months studied b) Moving sum of weighted count of earthquakes relative to SSE contours as a function of time (see Table 1). The moving sum is for 4 days. The shaded gray patch marks the duration of the 2014 SSE, with start and end times determined in Wallace et al. (2016).

4 Discussion

The relationship between seismicity and occurrence of SSEs around the world is not well understood. In the northern Hikurangi margin over the year 2014, one of these SSEs was recorded while a temporarynetwork of ocean bottom seismometers was deployed. This offshore array of seismometers in conjunction with the permanent seismic network of New Zealand enabled us to study the behavior of seismicity throughout the duration of the 2014 SSE. A detailed catalog of earthquakes is essential to study such relationships and to assist other seismological studies (such as seismic tomography, anisotropy, attenuation, among others) that depend on the earthquake detections and their seismic wave phase arrivals.

One of the potential advantages of using an automated method to pick arrivals and detect events is that the biases associated with an analyst (or multiple analysts) can be avoided (Allam & Ben-Zion, 2012; Diehl et al., 2009; Di Stefano et al., 2006). Consequently, temporal analyses of earthquake occurrence tend to be more reliable in automated earthquake catalogs than when performed on a manually built catalog. Our automated catalog throughout the 2014 SSE reveals further insights into the temporal and spatial distribution of seismic events during a regional slow slip event.

The detector and onset estimator program REST was used in this study to automatically generate an earthquake catalog. This method detected a total of 1739 hypocenters in the period between September 1st and October 31st 2014, 853 of which are considered well constrained. Over the same period, a manually built catalog detected a total of 265 events (Yarce et al., 2019), indicating that this automatic method can potentially detect at least 3 times more events than a manually built catalog. For events found by both manual and automatic picking, we found that the number of picks identified per event was also larger for the automatic method, with an average of 20 or more P and S arrivals per event compared to the number of phases picked manually. It is also worth noting that during the comparison of these autopicked events with our previous manually-picked catalog, we discovered that at least five of the previously reported earthquakes were in error. These 'false positive' events provide additional arguments for why an autopicking program may be preferable as the manual databases are prone to human error.

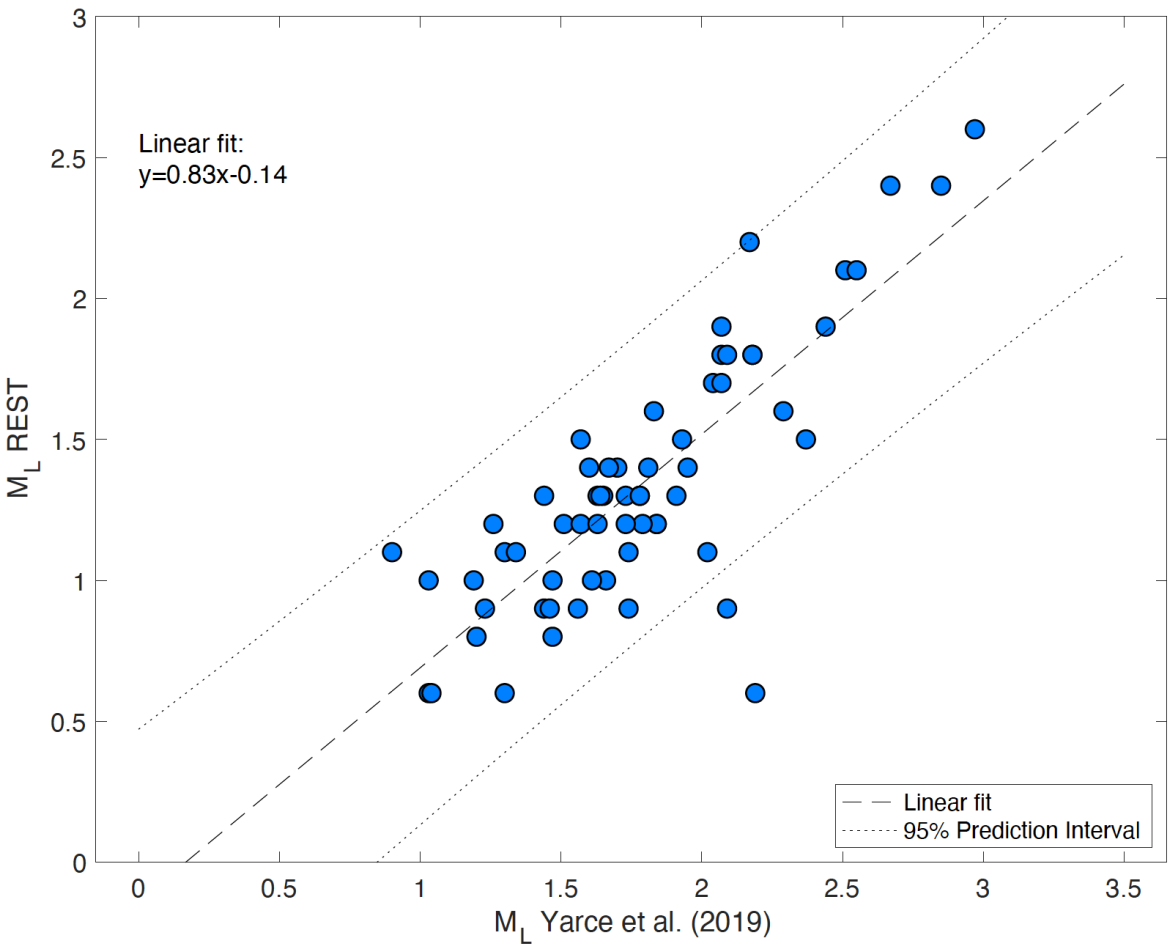

Figure 9: Distribution of magnitudes for earthquakes that are common to the automated (vertical axis) and manual (horizontal axis) catalogs. Dashed line shows the linear regression and the dotted line marks the bounds of 95% confidence interval bounds.

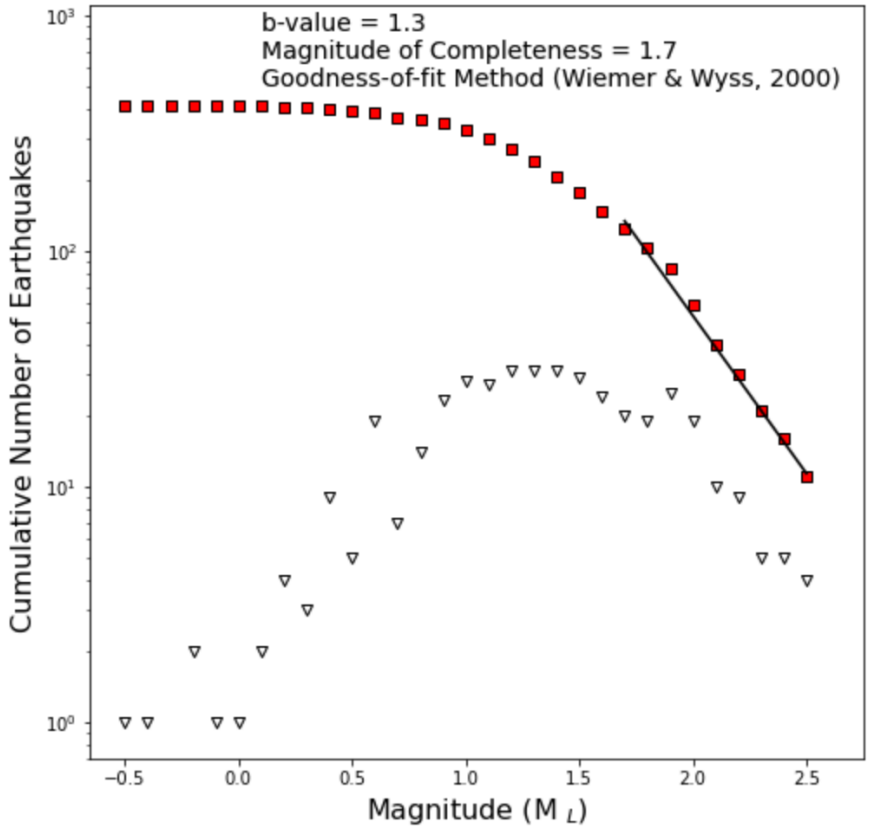

Figure 10: Frequency-magnitude relation for corrected magnitudes in automated earthquakes. Solid red squares mark the cumulative Gutenberg-Richter curve for the number of earthquakes with greater magnitude M_L. Open black triangles mark the curve for incremental values in 0.1 Log(M_L) magnitude unit bins. Black solid line shows the resulting b-value of 1.3.

Hypocenter locations for the high-quality 853 events registered using automated detection show similar patterns of previously-reported (e.g. Yarce et al. (2019)) seismicity and may be correlated with North Island fault traces. We note that our new catalog is showing these patterns with analysis of just two months of data, whereas the original study needed a full year of data. Our new autopicked catalog retains the microseismicity gap and is generally consistent with the spatial distribution of seismicity that was previously shown in manually-built catalogs (Figure 7 in Yarce et al., 2019) or catalogs that use template-matching or repeating earthquake techniques (e.g., the large number of earthquakes adjacent and downdip from seamounts in Figure 2 in Shaddox & Schwartz, 2019). Offshore seismicity in the automatic catalog also correlates with a cluster of earthquakes towards the down dip edge of a subducted seamount identified using magnetotellurics (Barker et al., 2018). The northeast-southwest linear trend of earthquakes towards the west of our study region may be associated with the Arahiki fault in the southern portion (Berryman et al., 2009) or with the Fernside fault in the northern portion of the lineation (Mazengarb, 1984) (see lines labeled AF and FF in Figure 5). The Arahiki fault lies subparallel to the Repongaere fault, a 4.5 km long active fault that may be connected with the Arahiki fault, with the most recent event recorded at c. 3400 yr BP (Berryman et al., 2009). The Fernside fault is an east-dipping active fault with a 1 km long scarp over the southern portion of the fault (Mazengarb, 1984). In summary, the use of an automatic method, as opposed to the manual picking method employed in previous studies, yielded results that are consistent with previously published catalogs (e.g. Shaddox & Schwartz, 2019; Todd et al., 2018; Yarce et al., 2019) but also expanded the detection such that the seismicity record potentially reveals active faults that have not been reported from prior seismic studies (Figure 5).

The automatic earthquake detection and location algorithm used in this study implemented the 3D velocity model of Yarce et al (2021) as opposed to the two 1D velocity models used in a previous study (Yarce et al., 2019). Systematic shifts in earthquake locations of hypocenters calculated with 1D versus 3D velocity models have been identified previously in other studies that targeted highly lateral heterogenous media such as other subduction zones or the San Andreas fault (Eberhart-Phillips & Michael, 1993;Matrullo et al., 2013; Johnson & Vincent, 2002). This study also found systematic shifts of earthquake locations

relative to the manual catalog with 1D velocity models, with most of the earthquakes shifting towards the west (or landwards) and towards shallower depths. Most likely these shifts are a result of mantle velocities (~8.2 km/s) determined at shallower depths (Yarce et al., 2021) in the onshore portion of our study area than used in the 1D velocity model applied by Yarce et al. (2019). For example, the onshore 1D velocity model was set to have mantle velocities at depths > 38 km, but seismic tomography imaging revealed that near the shore, mantle velocities can occur at depths as shallow as ~25 km (Yarce et al., 2021).

Taking advantage of the uniformity and consistency in automatic earthquake detection and localization, we analyzed the temporal and spatial record of earthquake occurrences relative to the 2014 SSE event. The results suggest that, during the SSE, there was an increase in the number of earthquakes weighted by their location relative to the SSE patch, growing in weighted occurrence over the course of, and mostly during roughly the second half of, the SSE (Figure 8). This increase in the rate of seismicity started a few days after the onset of the 2014 SSE (approximately on October 1st) and continued increasing until the end of the SSE (around October 10th). For several days after the termination of the SSE, the seismicity near the SSE decreases to background rates with small oscillations. Although the microearthquake seismicity per day decreases, the number of earthquakes after the end of the SSE remains high until mid-October 2014. During the two weeks following the end of the SSE the area under the curve in Figure 8b is around 1.8 times larger than the area under the curve between the start and end of the SSE. We also observe that the seismicity during the week after the SSE (Oct. 9 – 16, 2014) is almost as much as the cumulative weighted seismicity during the SSE (Sept. 23 – Oct. 9, 2014). Increases in the rate of seismicity or tremor activity associated with the 2014 SSE, with largest increases towards immediately or after the end of the slip event, have been previously reported for this area (Shaddox & Schwartz, 2019; Todd et al., 2018; Yarce et al., 2019; Iwasaki et al., 2022). Studies of other regions where shallow SSEs have been documented, such as the Nazca subduction zone in Ecuador, the Cocos subduction zone in Costa Rica, and the Nankai subduction zone in Japan, have shown that increases in the rate of seismicity often occur during SSE sequences and the associated earthquakes may use the same source faults (Jiang et al., 2017; Nakano et al., 2018; Vallée et al., 2013).

Finally, the Gutenberg-Richter frequency-magnitude relation based on the 451 events for which REST based estimates of magnitude were available shows a b-value of 1.3 corresponding to the linear portion of the slope, and a magnitude of completeness (M_C) of 1.7 (Figure 10). The application of quality control criteria on magnitude estimations resulted in our dataset of calculated magnitudes being only a subset of the total catalog, thus our auto-detector results are not directly comparable with the magnitude detection threshold of Yarce et al. (2019).

5 Conclusions

We tested an automatic seismic event detector as a tool to increase microearthquake detections and perform temporal analyses of earthquake occurrence. With the automated detection software we found three times as many events as were found in the same time period using manual methods. In addition to increasing the catalog of events by threefold, the automated method is uniformly applied and avoids possible analyst biases and inconsistencies. The auto-detected record of earthquakes revealed a possible temporal relationship between microseismicity and the cessation of the 2014 SSE, with an increase in weighted and raw occurrence of earthquakes throughout the duration of the SSE, remained high for two weeks after the SSE, thendecayed to background levels of seismicity. The expanded detection also reveals seismicity along active faults that have not been reported from other studies covering this time period. We recommend the future use of automated seismic event detection software to enhance catalog completeness, reduce analyst biases, and reveal underlying trends in microearthquake spatial and temporal patterns.

Acknowledgements

Support for data acquisition was provided by the U.S. National Science Foundation (NSF) grant 1333025, and subsequent analyses were funded by NSF grant 1551922. The ocean bottom seismic data were provided by instruments from the Ocean Bottom Seismic Instrument Center (https://obsic.whoi.edu/ - formerly known as OBSIP) funded by NSF, the Earthquake Research Institute (ERI) at the University of Tokyo, and New Zealand's GeoNet project. We greatly appreciate the work of the HOBITSS team of PIs,

students, and engineers that successfully deployed and recovered the ocean bottom instruments used for this study. We thank the Editor Claudio Faccenna, reviewer Cliff Thurber, and an anonymous reviewer for their constructive comments. The authors acknowledge that the data were acquired in an area that was first inhabited by the Māori and we reaffirm their contemporary and ancestral ties to this land first known as Aotearoa (New Zealand), specifically in the regions of Hikurangi, Maungapohatu, Tūranganui a Kiwa, and Te Māhia.

Open Research

Data Availability Statement

The raw seismic data from the HOBITSS experiment are archived at the Incorporate Research Institutions for Seismology Data Management Center (IRIS-DMC) with DOI: https://doi.org/10.7914/SN/YH_2014. The land seismic data are openly available through GeoNet (www.geonet.org.nz). The catalog of automated earthquakes hypocenters and the list of P- and S-wave arrivals for the two months around the 2014 slow slip event is openly available in Zenodo at https://doi.org/10.5281/zenodo.7274399. Some figures were plotted with Generic Mapping Tools (GMT) (Wessel & Smith, 1995; Wessel et al., 2019). The software used to calculate the magnitude of completeness and b-value is from EQcorrscan (Chamberlain et al., 2017).

REFERENCES

Allam, A. A., & Ben-Zion, Y. (2012). Seismic velocity structures in the southern California plate-boundary environment from double-difference tomography. *Geophysical Journal International*, *190*(2), 1181–1196. https://doi.org/10.1111/j.1365-246X.2012.05544.x

Barker, D. H. N., Henrys, S., Caratori Tontini, F., Barnes, P. M., Bassett, D., Todd, E. K., & Wallace, L. M. (2018). Geophysical Constraints on the Relationship Between Seamount Subduction, Slow Slip, and Tremor at the North Hikurangi Subduction Zone, New Zealand. *Geophysical Research Letters*, *45*(23), 12,804-12,813. https://doi.org/10.1029/2018GL080259

Berryman, K. R., Marden, M., Palmer, A., & Litchfield, N. (2009). Holocene rupture of the Repongaere Fault, Gisborne: Implications for Raukumara Peninsula deformation and impact on the Waipaoa Sedimentary System. *New Zealand Journal of Geology and Geophysics*, *52*(4), 335–347. https://doi.org/10.1080/00288306.2009.9518462

Chamberlain, C. J., Hopp, C. J., Boese, C. M., Warren-Smith, E., Chambers, D., Chu, S. X., Michailos, K., Townend, J. (2017) EQcorrscan: Repeating and near-repeating earthquake detection and analysis in Python. Seismological Research Letters.

Colella, H. V., Sit, S. M., Brudzinski, M. R., Graham, S. E., DeMets, C., Holtkamp, S. G., et al. (2017). Seismicity rate increases associated with slow slip episodes prior to the 2012 M w 7.4 Ometepec earthquake. *Earth and Planetary Science Letters*, *464*, 35–45. https://doi.org/10.1016/j.epsl.2016.12.032

Comte, D., Farias, M., Roecker, S. W., & Russo, R. (2019). The nature of the subduction wedge in an erosive margin: Insights from the analysis of aftershocks of the 2015 Mw 8.3 Illapel earthquake beneath the Chilean Coastal Range. *Earth and Planetary Science Letters*, *520*, 50–62. https://doi.org/10.1016/j.epsl.2019.05.033

Diehl, T., Deichmann, N., Kissling, E., & Husen, S. (2009). Automatic S-wave picker for local earthquake tomography. *Bulletin of the Seismological Society of America*, *99*(3), 1906–1920. https://doi.org/10.1785/0120080019

Dragert, H., Wang, K., & James, T. S. (2001). A silent slip event on the deeper Cascadia subduction interface. *Science*, *292*(5521), 1525–1528. https://doi.org/10.1126/science.1060152

Eberhart-Phillips, D., & Michael, A. J. (1993). Three-dimensional velocity structure, seismicity, and fault structure in the Parkfield region, central California. *Journal of Geophysical Research*, *98*(B9), 15737–15758. https://doi.org/10.1029/93jb01029

Havskov, J., & Ottemoller, L. (2010). *Routine data processing in earthquake seismology: With sample data, exercises and software*. *Routine Data Processing in Earthquake Seismology: With Sample Data, Exercises and Software*. Springer Netherlands. https://doi.org/10.1007/978-90-481-8697-6

Ikari, M. J. (2019). Laboratory slow slip events in natural geological materials. *Geophysical Journal International*, *218*(1), 354–387. https://doi.org/10.1093/gji/ggz143

Ito, Y., Hino, R., Kido, M., Fujimoto, H., Osada, Y., Inazu, D., et al. (2013). Episodic slow slip events in the Japan subduction zone before the 2011 Tohoku-Oki earthquake. *Tectonophysics*, *600*, 14–26.

https://doi.org/10.1016/j.tecto.2012.08.022

Iwasaki, Y., Mochizuki, K., Ishise, M., Todd, E. K., Schwartz, S. Y., Zal, H., et al. (2022). Continuous tremor activity with stable polarization direction following the 2014 large slow slip event in the Hikurangi subduction margin offshore New Zealand. *Journal of Geophysical Research: Solid Earth*, 127, e2021JB022161. https://doi.org/10.1029/2021JB022161

Jiang, Y., Liu, Z., Davis, E. E., Schwartz, S. Y., Dixon, T. H., Voss, N., et al. (2017). Strain release at the trench during shallow slow slip: The example of Nicoya Peninsula, Costa Rica. *Geophysical Research Letters*, *44*(10), 4846–4854. https://doi.org/10.1002/2017GL072803

Johnson, M., & Vincent, C. (2002). Development and Testing of a 3D Velocity Model for Improved Event Location: A Case Study for the India-Pakistan Region. *Bulletin of the Seismological Society of America*, *92*(8), 2893–2910. https://doi.org/10.1785/0120010111

Kushnir, A. F., Lapshin, V. M., Pinsky, V. I., & Fyen, J. (1990). Statistically optimal event detection using small array data. *Bulletin of the Seismological Society of America*, *80*(6B), 1934–1950. https://doi.org/10.1785/BSSA08006B1934

Langridge, R.M., Ries, W.F., Litchfield, N.J., Villamor, P., Van Dissen, R.J., Barrell, D.J.A., Rattenbury, M.S., Heron, D.W., Haubrock, S., Townsend, D.B., Lee, J.M., Berryman, K.R., Nicol, A., Cox, S.C., Stirling, M.W. (2016). The New Zealand Active Faults Database. *New Zealand Journal of Geology and Geophysics 59:* 86-96. doi: 0.1080/00288306.2015.1112818.

Lanza, F., Chamberlain, C. J., Jacobs, K., Warren-Smith, E., Godfrey, H. J., Kortink, M., et al. (2019). Crustal Fault Connectivity of the Mw 7.8 2016 Kaikōura Earthquake Constrained by Aftershock Relocations. *Geophysical Research Letters*, *46*(12), 6487–6496. https://doi.org/10.1029/2019GL082780

Matrullo, E., De Matteis, R., Satriano, C., Amoroso, O., & Zollo, A. (2013). An improved 1-D seismic velocity model for seismological studies in the Campania–Lucania region (Southern Italy). *Geophysical Journal International*, *195*(1), 460–473. https://doi.org/10.1093/gji/ggt224

Mazengarb, C. (1984). The Fernside Fault: an active normal fault, Raukumara Peninsula, New Zealand. *New Zealand Geological Survey Record*, 98–103. Retrieved from https://www.researchgate.net/publication/280977091

Merrill, R. J., M. G. Bostock, S. M. Peacock, A. J. Schaeffer, and S. W. Roecker (2022). Complex Structure in the Nootka Fault Zone Revealed by Double-Difference Tomography and a New Earthquake Catalog, *Geochemisty, Geophysics, Geosystems, 23, 2,* https://doi.org/10.1029/2021GC010205

Nakano, M., Hori, T., Araki, E., Kodaira, S., & Ide, S. (2018). Shallow very-low-frequency earthquakes accompany slow slip events in the Nankai subduction zone /704/2151/210 /704/2151/508 article. *Nature Communications*, *9*(1), 1–8. https://doi.org/10.1038/s41467-018-03431-5

Pisarenko, V.F., A. F. Kushnir, and I. V. Savin, Statistical adaptive algorithms for estimation of onset moments of seismic phases, Physics of the Earth and Planetary Interiors, ISSN: 0031-9201, 47C, 4-10, 1987, doi: 10.1016/0031-9201(87)90062-8.

Rawles, C., & Thurber, C. H. (2015). A non-parametric method for automatic determination of P -wave

and S -wave arrival times: application to local micro earthquakes. *Geophysical Journal International*, *202*(2), 1164–1179. https://doi.org/10.1093/gji/ggv218

Ristau, J., Harte, D., & Salichon, J. (2016). A Revised Local Magnitude (M_L) Scale for New Zealand Earthquakes. *Bulletin of the Seismological Society of America*, *106*(2), 398–407. https://doi.org/10.1785/0120150293

Roecker, S, A Maharaj, S Meyers, and D Comte (2021), Double differencing by demeaning: applications to hypocenter location and wavespeed tomography, Bulletin of the Seismological Society of America 111 (3), 1234-1247.

Roecker, S. W., Thurber, C. H., Roberts, K., & Powell, L. (2006). Refining the image of the San Andreas Fault near Parkfield, California using a finite difference travel time computation technique. *Tectonophysics*, *426*(1–2), 189–205. https://doi.org/10.1016/J.TECTO.2006.02.026

Ross, Z. E., Meier, M. A., & Hauksson, E. (2018). P Wave Arrival Picking and First-Motion Polarity Determination With Deep Learning. *Journal of Geophysical Research: Solid Earth*, *123*(6), 5120–5129. https://doi.org/10.1029/2017JB015251

Schwartz, S. Y., & Rokosky, J. M. (2007). Slow slip events and seismic tremor at circum-Pacific subduction zones. *Reviews of Geophysics*, *45*(3), n/a-n/a. https://doi.org/10.1029/2006RG000208

Shaddox, H. R., & Schwartz, S. Y. (2019). Subducted seamount diverts shallow slow slip to the forearc of the northern Hikurangi subduction zone, New Zealand. *Geology*, *47*. https://doi.org/10.1130/g45810.1

Di Stefano, R., Aldersons, F., Kissling, E., Baccheschi, P., Chiarabba, C., & Giardini, D. (2006). Automatic seismic phase picking and consistent observation error assessment: Application to the Italian seismicity. *Geophysical Journal International*, *165*(1), 121–134. https://doi.org/10.1111/j.1365-246X.2005.02799.x

Thurber, C. H., Lanza, F., and Roecker, S. W. (2017). Application of a Hybrid Detection and Location Scheme to Volcanic Systems. *AGUFM*, *2017*, S13B-0645.

Todd, E. K., Schwartz, S. Y., Mochizuki, K., Wallace, L. M., Sheehan, A. F., Webb, S. C., et al. (2018). Earthquakes and Tremor Linked to Seamount Subduction During Shallow Slow Slip at the Hikurangi Margin, New Zealand. *Journal of Geophysical Research: Solid Earth*, *123*(8), 6769–6783. https://doi.org/10.1029/2018JB016136

Vallée, M., Nocquet, J.-M., Battaglia, J., Font, Y., Segovia, M., Régnier, M., et al. (2013). Intense interface seismicity triggered by a shallow slow slip event in the Central Ecuador subduction zone. *Journal of Geophysical Research: Solid Earth*, *118*(6), 2965–2981. https://doi.org/10.1002/jgrb.50216

Wallace, L. M. (2020). Slow Slip Events in New Zealand. *Annual Review of Earth and Planetary Sciences*, *48*(1), annurev-earth-071719-055104. https://doi.org/10.1146/annurev-earth-071719-055104

Wallace, L. M., Webb, S. C., Ito, Y., Mochizuki, K., Hino, R., Henrys, S., et al. (2016). Slow slip near the trench at the Hikurangi subduction zone, New Zealand. *Science*, *352*(6286), 701–704. https://doi.org/10.1126/science.aaf2349

Wessel, P., Luis, J. F., Uieda, L., Scharroo, R., Wobbe, F., Smith, W. H. F., & Tian, D. (2019). The generic mapping tools version 6. *Geochemistry, Geophysics, Geosystems*, *20*(11), 5556– 5564. https://doi.org/10.1029/2019gc008515

Wessel, P., & Smith, W. H. F. (1995). New version of the generic mapping tools, Eos. *Transactions - American Geophysical Union*, *76* (33), 329.

Wiemer, S., & M. Wyss (2000). Minimum magnitude of completeness in earthquake catalogs: Examples from Alaska, the Western United States, and Japan, *Bulletin of the Seismological Society of America*, 90 (4), 859-869, doi: https://doi.org/10.1785/0119990114.

Williams, C. A., Eberhart-Phillips, D., Bannister, S. C., Barker, D. H. N., Henrys, S. A., Reyners, M., & Sutherland, R. (2013). Revised Interface Geometry for the Hikurangi Subduction Zone, New Zealand. *Seismological Research Letters*, *84*(6), 1066–1073. https://doi.org/10.1785/0220130035

Yarce, J., Sheehan, A. F., Nakai, J. S., Schwartz, S. Y., Mochizuki, K., Savage, M. K. K., et al. (2019). Seismicity at the Northern Hikurangi Margin, New Zealand, and Investigation of the Potential Spatial and Temporal Relationships with a Shallow Slow Slip Event. *Journal of Geophysical Research: Solid Earth*, *124*(5), 4751–4766. https://doi.org/10.1029/2018JB017211

Yarce, J., Sheehan, A., Roecker, S., & Mochizuki, K. (2021). Seismic velocity heterogeneity of the Hikurangi subduction margin, New Zealand: Elevated pore pressures in a region with repeating slow slip events. Journal of Geophysical Research: Solid Earth, 126, e2020JB021605. https://doi.org/10.1029/2020JB021605